

Characteristics Analysis of Double-Sided Permanent Magnet Linear Synchronous Motor with Three-Phase Toroidal Windings

Xiaobao Chai¹, Jikai Si¹, Yihua Hu², Yingsheng Li³, and Dongshu Wang¹

¹Department of Electrical Engineering, Zhengzhou University, Zhengzhou, 450001, China
 xbcstu@126.com, sijikai@zzu.edu.cn, wangdongshu@zzu.edu.cn

²Department of Electronic Engineering, University of York, York, YO 10 5DD, U.K.
 yihua.hu@york.ac.uk

³Zhengzhou Runhua Intelligent Equipment Co., Ltd., Zhengzhou, 450004, China
 xdlys@vip.sina.com

Abstract — This paper proposes three-phase 120° phase belt toroidal windings (120°-TW) and are applied in a double-sided permanent magnet linear synchronous motor (DSPMLSM), in which the incoming ends of all coils are on the same side and have the same incoming direction. First, the structure of the proposed motor is introduced and its operation principle is analyzed by describing the variation in the armature magnet field versus time. Second, based on the similar volume, magnetic load and electrical load, the initial parameters of the DSPMLSM with different winding arrangements are presented. Then, the finite-element models (FEMs) of the DSPMLSM with 120°-TW (120°-TWDSPMLSM) and traditional toroidal windings (TTW) are established to analyze the distribution of magnetic field, back electromotive force (back-EMF), detent force, thrust, efficiency and so on. Besides, the primary optimization of the detent force is designed. Finally, the results show that the thrust density and efficiency of the 120°-TWDSPMLSM is higher than that of DSPMLSM with TTW (TTWDSPMLSM).

Index Terms — Character analysis, double-sided permanent magnet linear synchronous motor, operation principle, three-phase 120° phase belt toroidal windings, thrust density.

I. INTRODUCTION

Double-sided permanent magnet (PM) linear synchronous motors (DSPMLSMs) are widely used in various industrial applications and daily life due to advantages of simple structure, high thrust density, low maintenance cost and unilateral magnetic force in recent years [1-4]. However, in limited space applications, the thrust density of the DSPMLSM is expected to be higher. Therefore, many researchers worldwide are pursuing the goal of improving the thrust density of the DSPMLSM

[5-7].

Researchers have done much excellent work to improve the thrust density, which can be summarized four improvement techniques. The first technique adds magnetic field modulator blocks, the thrust density is improved by adopting the method magnetic field modulation in [8-9]. The second technique improve the thrust density by changing the PM arrangement, the thrust density is improved by adopting the structure of serial magnetic circuit [10-11]. The third technique is to change the cooling mode, the force-air cooling and water-cooling method are adopted, which improves the thrust density [12-13]. The last technique changes the winding configurations, and changing winding configurations are more simple comparing with these alternatives. The concentrated and full-pitch windings are applied in [14], but the sinusoidal waveform of back electromotive force (back-EMF) is poor and has some higher-order harmonics. In [15] the DSPMLSM adopting distributed and short-pitch windings are designed and reduces the harmonic content of back-EMF, but it has great trouble to manufacture the motor. The DSPMLSM with fractional-slot concentrated windings is proposed and is suitable for limited space applications due to small size, high efficiency and easy manufacture [16-17]. However, the winding factor of the fractional-slot concentrated winding is relatively low, which has negative effects on the amplitude of back-EMF and thrust density. To improve the thrust density, the DSPMLSM with traditional toroidal windings (TTWDSPMLSM) is proposed in [18], and the thrust density of the TTWDSPMLSM is higher than the DSPMLSM with fractional-slot concentrated windings. In [19], the torque density of a direct-drive permanent magnet synchronous motor with 120° phase belt toroidal windings is higher than that with traditional toroidal windings. The 120°-TW also can be applied to the DSPMLSM to improve

the thrust density.

Summarized the above topology structures, this paper presents a double-sided permanent magnet linear synchronous motor with three-phase 120° phase belt toroidal windings (120°-TWDSPMLSM), in which the incoming ends of all coils are on the same side and have the same incoming direction. The structure and the winding connected method of the 120°-TWDSPMLSM is introduced in Section II. Besides, its operating principle is analyzed. In Section III, the design of the 120°-TWDSPMLSM is illustrated in detail. Then, the finite element models (FEMs) of the two motors are established in Section IV. Comprehensive comparisons between the 120°-TWDSPMLSM and TTWDSPMLSM from the aspect of operating characteristic are presented, and the primary optimization of the detent force is designed. Finally, a brief summary of this paper as well as the directions for future research work are proposed in Section V.

II. STRUCTRE AND OPERATION PRINCIPLE OF THE 120°-TWDSPMLSM

A. Structure of the 120°-TWDSPMLSM

The structure sketches of the 120°-TWDSPMLSM and TTWDSPMLSM are shown in Fig. 1 and Fig. 2, respectively. It can be seen from Fig. 1 and Fig. 2 that both the two motors consist of one primary and two secondary components. Besides, in the secondary, the permanent magnets of the two motors are arranged alternately along the moving direction. The prominent advantage for the double-sided secondary topology is that the toroidal windings can be adopted.

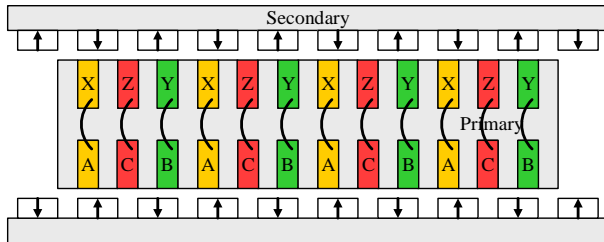


Fig. 1. Structure sketch of the 120°-TWDSPMLSM.

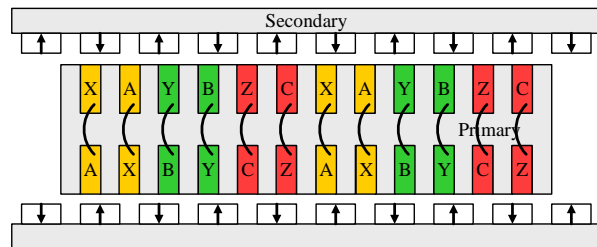


Fig. 2. Structure sketch of the TTWDSPMLSM.

Moreover, it could be also seen that the 120°-

TWDSPMLSM is different with the TTWDSPMLSM, and the differences between the two motors are found as following.

(1) The unit motor of the 120°-TWDSPMLSM has three slots and two poles, as shown in Fig. 1. However, it can be found from Fig. 2 that the unit motor of the TTWDSPMLSM has six slots and four poles.

(2) It should be noted that all incoming line ends of the 120°-TW are on the same side and have the same incoming direction, however, the incoming line ends of the TTW are on both side of the motor.

B. Operation principle of the 120°-TWDSPMLSM

A three-slot unit motor is selected as an example to clearly clarify the operation principle of the 120°-TWDSPMLSM in this subsection. Three-phase current supplied to the three-phase windings are shown in Fig. 3. The current directions of the three-phase winding coils at different time are shown in Table 1, where ‘+’ and ‘-’ represent that the current flows into and out the windings, respectively. Based on the distributions of the three-phase winding currents at different times and the faraday law of electromagnetic induction, the armature magnetic field distribution in each moment is described in detail, as shown in Fig. 4, where ‘+’ and ‘•’ represent that the current flows into and out the windings, respectively.

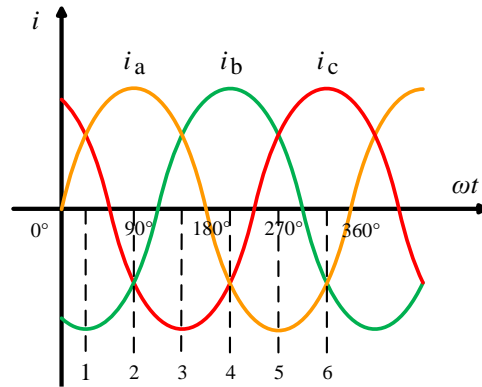


Fig. 3. Current waveforms supplied to three-phase windings.

Table 1: Current directions of three-phase winding coils versus time

Phase	Time					
	1	2	3	4	5	6
A	+	+	+	-	-	-
B	-	-	+	+	+	-
C	+	-	-	-	+	+

The variation of the magnetic poles can be found from Fig. 4 as following.

(1) Compared with the magnetic fields at Time 1,

Time 2 shows that the N pole of the armature magnetic fields has no movement, but the S pole moves 120° in the left direction.

(2) The N pole of the armature magnetic fields at Time 3 has moved by 120° in the left direction, while the S pole has no movement compared with that at Time 2.

(3) Compared with the magnetic fields at Time 3, Time 4 shows that the N pole of the armature magnetic fields does not move, but the S pole moves 120° in the left direction.

(4) The N pole of the armature magnetic fields at Time 5 has moved by 120° in the left direction, while the S pole does not move compared with that at Time 4.

(5) Compared with the magnetic fields at Time 5, Time 6 shows that the N pole of the armature magnetic fields has no movement, but the S pole moves 120° in the left direction.

As a result, it can be concluded that the armature magnetic field of the three-slot unit motor forms a pair of poles and changes periodically.

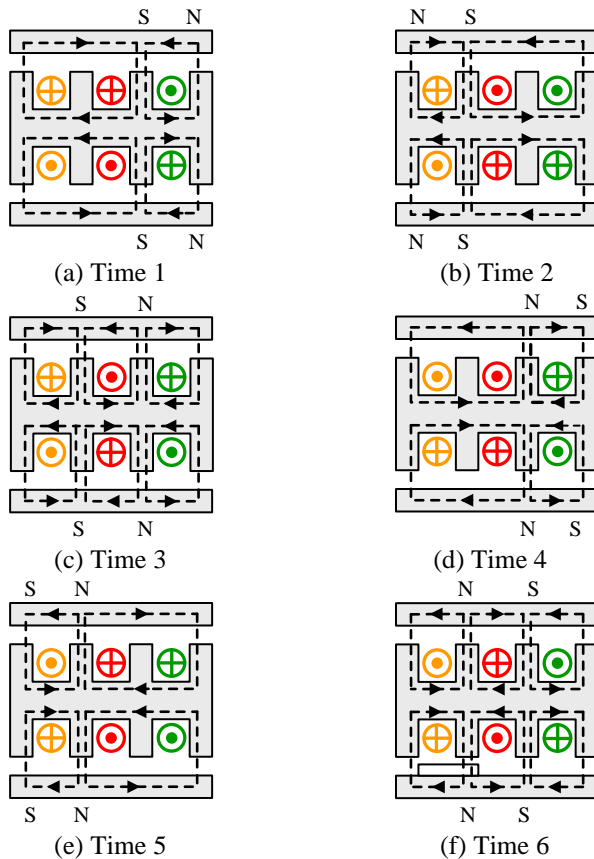


Fig. 4. Armature magnetic field versus time.

III. INITIAL PARAMETER OF THE 120° -TTWDSPLMSM AND TTWDSPLMSM

To verify the feasibility of the proposed motor, the 120° -TTWDSPLMSM is designed and compared with

the TTWDSPLMSM. In [18], the main dimensional parameters of two motors are presented in detail. The design needs to meet the following criteria to ensure a fair comparison.

(1) The two motors have the similar air-gap flux density.

(2) The wire diameter of the 120° -TTWDSPLMSM must be consistent with that of TTWDSPLMSM.

(3) The two motors have the same moving speed.

(4) The two motors are excited by a current source and has the same electrical load.

(5) The same materials are adopted in the corresponding parts of the two motors.

(6) The same mesh refine is adopted.

Based on the principles above, the initial parameters of the 120° -TTWDSPLMSM and TTWDSPLMSM are summarized in Table 2.

Table 2: Initial parameters of the 120° -TTWDSPLMSM and TTWDSPLMSM

Items	120° -TTWDSPLMSM	TTWDSPLMSM
Pole numbers	8	8
Slot numbers	12	12
Pole pitch (mm)	16.5	16.5
PM width (mm)	12.4	12.4
PM thickness (mm)	3	3
Air-gap length (mm)	1	1
Slot pitch (mm)	11	11
Slot width (mm)	6	6
Teeth width (mm)	5	5
Coil number/phase	4	4
Turns/coil	135	135
Primary width (mm)	60	60
synchronous speed (m/s)	0.33	0.33

IV. CHARACTERISTIC ANALYSIS OF THE 120° -TTWDSPLMSM AND TTWDSPLMSM

With the parameters reported in Table 2, the Finite Element Models (FEMs) of the two motors are established to compare and analyze the electromagnetic characteristics under no-load and on load conditions.

A. No-load characteristic

To analyze the internal magnetic field intuitively and effectively, the magnetic flux distribution, air-gap flux density, back-EMF and detent force under no-load condition of the two motors are compared and analyzed.

The no-load magnet flux distributions of the two motors are same, because the flux generated by the permanent magnet is independent of the winding arrangements. Figure 5 shows the no-load magnetic flux

distribution and the approximate closed loops in the 1/4 model of the two motors.

The two motors can generate parallel magnetic circuits due to the corresponding magnets on the two sides that have the same polarity facing the primary. In addition, it can be seen that there are three types of paths in 120°-TWDSPMLSM and TTWDSPLSM, which are called the long loop, middle loop, and short loop in this paper, respectively. The magnetic flux lines of the long loop and middle loop are close through the secondary yoke, the air gap, the primary teeth and the primary yoke along the magnetization direction to form a loop, which is called effective magnet flux. By contrast, the magnetic flux lines of the short loop do not pass through the primary yoke, which is called ineffective magnet flux.

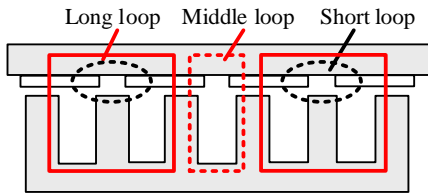


Fig. 5. The no-load magnetic flux distribution and the approximate closed loops in 120°-TWDSPMLSM and TTWDSPLSM (1/4 model).

The no-load air-gap flux density waveforms and the corresponding harmonics distribution of the two motors within two pole pitches are presented in Fig. 6.

It can be seen that the air-gap flux density waveforms of the 120°-TWDSPMLSM is consistent with the air-gap flux density waveforms of the TTWDSPLSM. By Fourier analysis, the amplitudes of the fundamental component of the air-gap flux density in the 120°-TWDSPMLSM and TTWDSPLSM both are 0.78T.

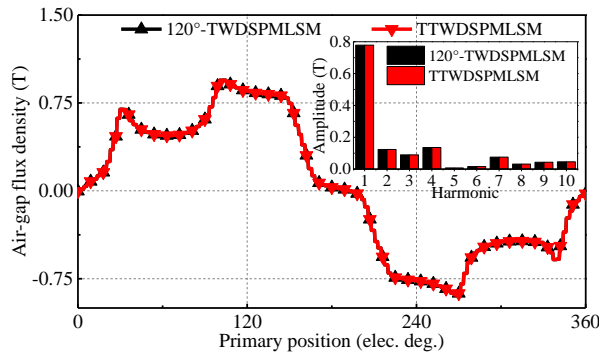


Fig. 6. No-load air-gap flux density waveforms of the 120°-TWDSPMLSM and TTWDSPLSM.

The no-load back-EMF waveforms and the corresponding harmonics distribution of the 120°-

TWDSPLSM and TTWDSPLSM at the same speed are presented in Fig. 7.

By the Fourier analysis, it can be seen that the no-load back-EMF of the two motors have little even harmonics. Moreover, the amplitudes of the fundamental component of the no-load back-EMF of the 120°-TWDSPLSM (17.24V) is higher 18.98% than that of TTWDSPLSM (14.49V). The total harmonic distortions (THDs) of back-EMF of the 120°-TWDSPLSM and TTWDSPLSM are 2.63% and 1.80%, respectively. And the THDs of back-EMF of the 120°-TWDSPLSM is a little higher than that of the TTWDSPLSM.

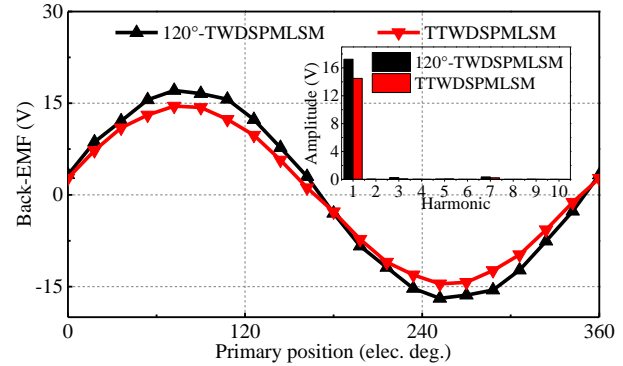


Fig. 7. No-load back-EMF waveforms of the 120°-TWDSPLSM and TTWDSPLSM.

The fundamental harmonic amplitude of no-load back-EMF of one side of a coil of the 120°-TWDSPLSM can be expressed as [20]:

$$E_1 = NBlv, \tag{1}$$

where, N is the number of the conductor, B is the fundamental harmonic amplitude of the air gap flux density, l is conductor effective length, v is the speed of the motor.

Since each E_1 is superposition the same direction. Therefore, the fundamental harmonic amplitude of no-load back-EMF of the 120°-TWDSPLSM can be further expressed as:

$$E = zE_1 = zNBlv, \tag{2}$$

where, z is the slot number.

According to formula (2) and the parameters of the 120°-TWDSPLSM in Table 2, it is can be calculated that the E is equal to 16.68 V. The result has small deviation comparing with simulation result (17.24 V), but the error (3.35%) is less than 5%. Thus, the EFA is credible.

The detent force, which can be divided into the end force and cogging force, can cause vibration and noise of DSPMLSM. therefore, it is a key problem to be considered and solved in the design and manufacture of high performance DSPMLSM. The detent force F_{dent} is shown in formulas (3-5) [21]:

$$F_{dent} = F_{end} + F_{slot}, \quad (3)$$

$$F_{end} = \frac{2K_c \delta \Phi_m^2}{\mu_0 k_1 \tau^2 l} \frac{4}{\pi} \sum_{n=1}^{\infty} \frac{1}{n} (\sin n \frac{2\pi}{\tau} x), \quad (4)$$

$$F_{slot} = \frac{\pi^2 z l}{2\mu_0 p \tau} (\frac{p\tau}{\pi} + \delta^2) \sum_{n=1}^{\infty} n G_n B_{nz/2p} \sin(\frac{2n\pi z}{p\tau} x), \quad (5)$$

where K_c is the Carter's coefficient, δ is the length of air-gap, Φ_m is the maximum flux amplitude across the end of primary, μ_0 is the permeability of vacuum, k_1 is the flux compression coefficient, τ is the pole pitch, $B_{nz/2p}$ is the $nz/2p$ -th harmonic of residual magnetism. G_n is the n -th harmonic of permeance, F_{end} is the detent force, F_{slot} is the cogging force.

Based on the finite element models and formulas (3-5), the detent force values of the two motors are calculated, as shown in Fig. 8. It can be seen that the peak-to-peak values of detent force of the two motors both are 100.84 N. According to the formulas (3-5), since all parameters are the same, the detent forces of the two motors are equal. The detent force is large, and it is important to minimize the detent force in a later subsection.

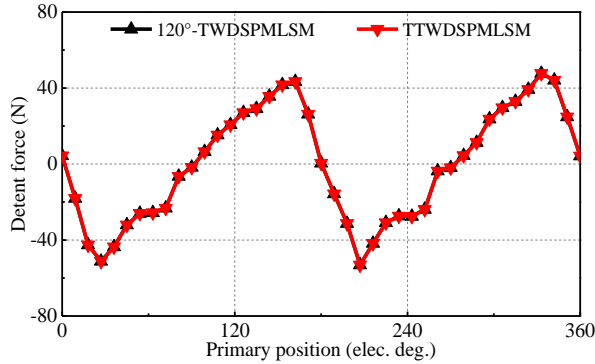


Fig. 8. Detent force waveforms of the 120°-TWDSPMLSM and TTWDSPMLSM under no load.

B. Load characteristic

The average thrust F is shown in formula (6) [22]:

$$F = \frac{3EI \cos \varphi}{\sqrt{2}v}, \quad (6)$$

where, I is the average value of phase current, $\cos \varphi$ is the power factor.

The thrust waveforms of the two motors at the same current density (6.0 A/mm²) are shown in Fig. 9. It can be seen that the average thrust of the 120°-TWDSPMLSM and TTWDSPMLSM are respectively 250.40 N and 205.88 N. Besides, the thrust density of the 120°-TWDSPMLSM (4.84×10^2 kN/m³) is 21.62% higher than that of the TTWDSPMLSM (3.98×10^2 kN/m³).

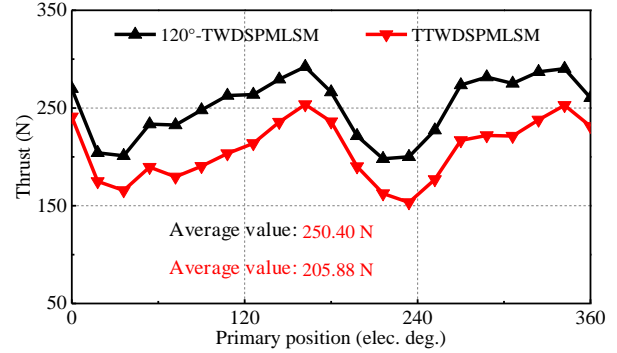


Fig. 9. Thrust waveforms of the 120°-TWDSPMLSM and TTWDSPMLSM on load.

According to the formula (6), it can be calculated that the average thrust F of the 120°-TWDSPMLSM is equal to 254.12 N. The simulation result broadly concurs with (6), with the small deviation which can be attributed to the harmonic which is ignored in (6), whereas is considered in the FEM simulation model.

Additionally, the thrust ripple F_{ripple} is shown in formal (7) [18]:

$$F_{ripple} = \frac{F_{max} - F_{min}}{F_{av}}, \quad (7)$$

where F_{max} , F_{min} , and F_{av} are the maximum, minimum and average value of the thrust, respectively.

The thrust ripples of the 120°-TWDSPMLSM and TTWDSPMLSM are 37.60% and 48.70%, respectively. Based on the above of detent force, it can be known that the main cause of thrust ripple is too large detent force. Therefore, in the next work, to reduced thrust ripple, it is important to minimize the detent force.

The Table 3 presents the losses and efficiency of the two motors.

Table 3: Losses and efficiency

Items	120°-TW DSPMLSM	TTW DSPMLSM
Output power (W)	82.63	67.94
Iron loss (W)	0.37	0.37
Copper loss (W)	81.89	81.89
Efficiency	50.11%	45.23%

It can be found that the output power of the 120°-TWDSPMLSM and TTWDSPMLSM are 82.63 W and 67.94 W, respectively. The copper losses of the two motors are same (81.89 W), because the number of conductors and the wire diameter are same in the two motors. Besides, the iron losses of the 120°-TWDSPMLSM and TTWDSPMLSM are both 0.37 W. the iron losses are lower than the copper losses of the two motors, which is negligible due to the frequency is 10 Hz. Therefore, the losses of the two motors are

mainly copper losses. The efficiency of the 120°-TWDSPMLSM and TTW DSPMLSM is 50.11% and 45.23%, respectively. Therefore, the efficiency of the 120°-TW DSPMLSM increases by 4.88%.

Figure 10 shows the thrust-current angle characteristic of the 120°-TW DSPMLSM and TTW DSPMLSM.

It should be noted that the current angle indicates the relative angle between the current phasor and the d-axis. The change of current angle affects the amplitude of q-axis current (I_q). Then increasing I_q can lead to the increment of the average thrust. If the current angle is between 0 and 90 elec. deg., I_q increases with the current angle. On the contrary, if it is between 90 and 180 elec. deg., I_q decreases as the current angle increases. When it is 90 elec. deg., I_q is injected only, i.e., the amplitude of d-axis current (I_d) is equal to 0 A. The motors achieve maximum thrust.

Therefore, when the current angle is between 0 and 180 elec. deg., the average thrust increases first and then decreases.

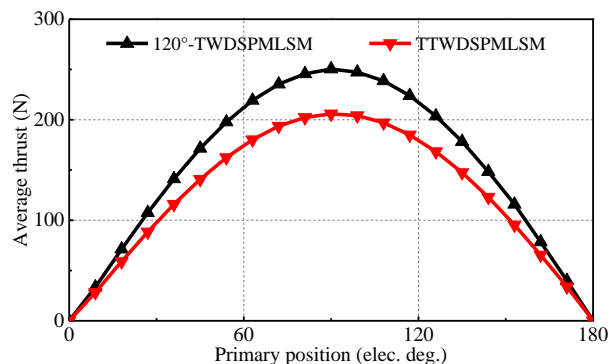


Fig. 10. Thrust-current angle characteristic of the 120°-TW DSPMLSM and TTW DSPMLSM.

Figure 11 shows the waveforms of the average thrust versus current density in two motors.

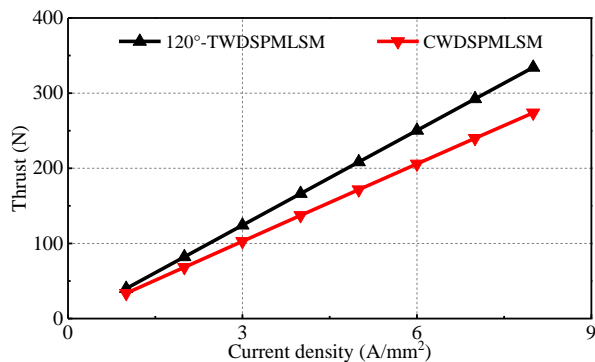


Fig. 11. Thrust versus current density.

It can be found that the average thrust of the 120°-

TW DSPMLSM is always larger than that of TTW DSPMLSM. Moreover, the average thrust of the two motors both increase linearly with the armature current density.

The waveforms of the loss versus frequency in the two motors are shown in Fig. 12.

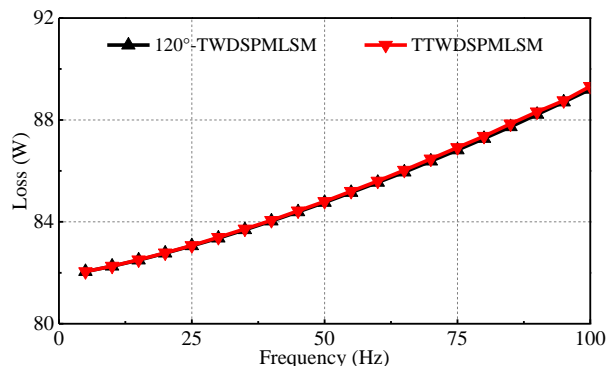


Fig. 12. Loss versus frequency.

It can be seen the losses of the two motors increase with frequency. Moreover, it can be found that the losses of the 120°-TW DSPMLSM and TTW DSPMLSM are same in various frequencies.

Figure 13 shows the waveforms of the efficiency versus frequency in the two motors.

It can be seen that the efficiencies of the two motors increase with the frequency and tend to be stable, finally. Besides, the efficiency of the 120°-TW DSPMLSM is higher than that of TTW DSPMLSM in various frequencies.

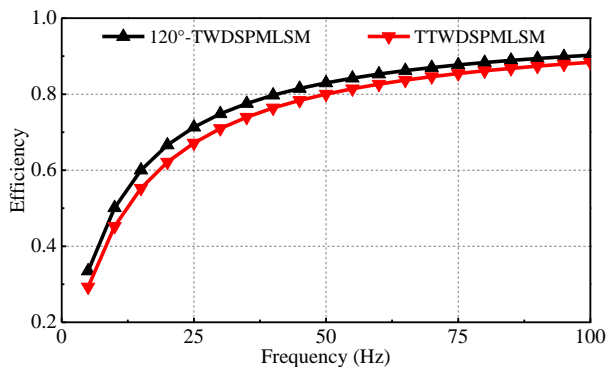


Fig. 13. Efficiency versus frequency.

C. Optimization of the detent force

The primary optimization of the detent force of the two motor is shown in Table 4.

As shown in the Table 4, the different length of the end tooth corresponds to the different value of the detent force. While the length of the end tooth is 6.0mm, the detent force is 100.84N. After optimization, it drops to

51.50N, when the length of end tooth is 8.0mm, which means that 48.92% of detent force can be reduced by changing the length of end tooth.

Table 4: Length of end tooth

Length of end tooth (mm)	5.5	6.0	6.5	7.0
Detent force (N)	103.77	100.84	92.25	79.46
Length of end tooth (mm)	7.5	8.0	8.5	9.0
Detent force (N)	67.64	51.49	69.10	83.40

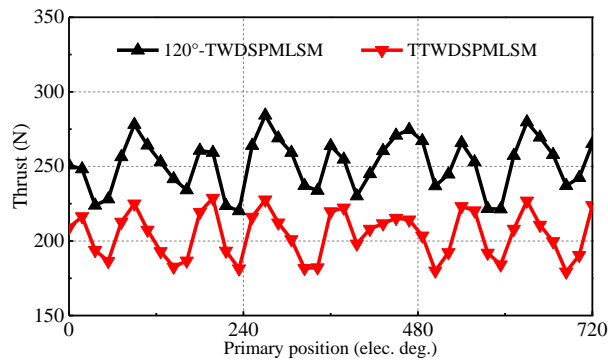


Fig. 14. Thrust waveforms of the 120°-TWDSPLSM and TTWDSPLSM on load.

The primary optimization waveforms of the thrust of the two motors are shown in Fig. 14. By primary optimization, it can be seen that the thrust ripples of the 120°-TWDSPLSM and TTWDSPLSM are 25.32% and 23.73%, respectively. Therefore, the thrust ripples of the 120°-TWDSPLSM and TTWDSPLSM can be reduced by 12.28% and 24.97% by changing the length of the end tooth, respectively.

D. FEA credibility and 120°-TW reasonableness validation

In order to verify the credible finite element analysis method and the reason of the proposed winding configuration (120°-TW), a permanent magnet rotation motor (PMRM) with the same 120°-TW can be used in the experiment. Figure 15 shows the prototype of the PMRM with 120°-TW (120°-TWPMRG), which includes the pedestal, rotor, stator yoke and 120°-TW. Figure 16 shows the corresponding test platform for the motor.

Figure 17 shows the comparison of the no-load back-EMF between EFA and the experiment at the constant linear velocity of 1 krpm. Figure 18 shows the comparison of the torque between FEA and the experiment at different current.

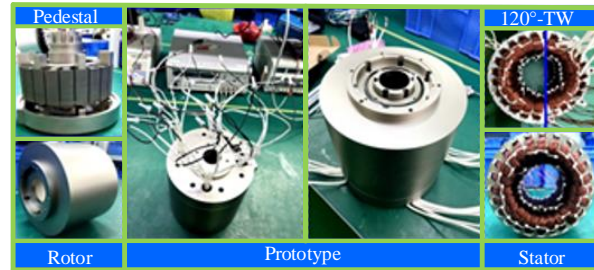


Fig. 15. Prototype of the 120°-TWPMRM.



Fig. 16 Test platform.

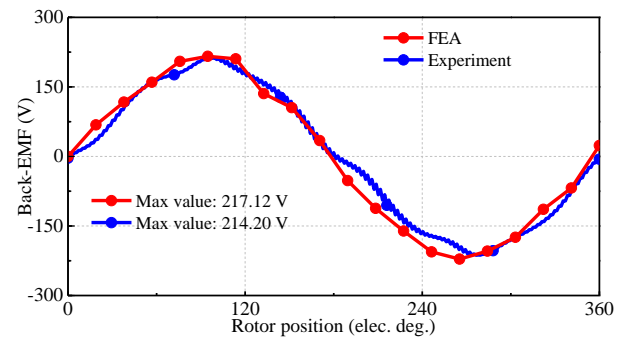


Fig. 17. Comparison of the no-load back-EMF between FEA and experiment.

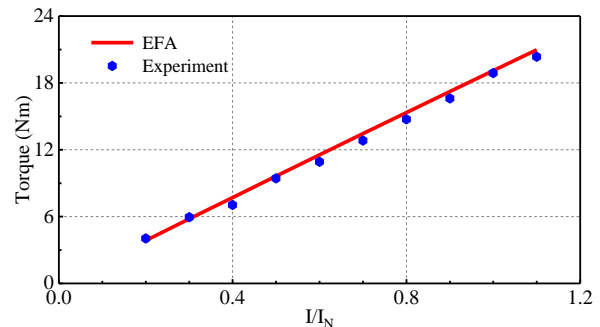


Fig. 18. Comparison of the torque between FEA and experiment at different current.

It can be seen that the no-load back-EMF obtained by FEA agrees with the experimental ones, which demonstrated the FEA method used to analyze the performance is accurate. Therefore, the analysis results obtained by the same analysis method (FEA) are credible in this paper.

V. CONCLUSION

This paper presented a 120°-TWDSPLSM, which has simple structure, high thrust density. The main work is focused on the characteristic analysis and comparison of the 120°-TWDSPLSM and TTWDSPLSM. The structure of the proposed motor is introduced and operation principle is clarified. Additionally, the key operating characteristics of the two motors are analyzed and compared. Moreover, the detent forces of two motors are preliminarily optimized. The comparison results validate the reasonability of the 120°-TWDSPLSM and exhibit the proposed motor possesses some advantages which can be concluded as below.

(1) The back-EMFs of the 120°-TWDSPLSM is higher 18.98% than that of the TTWDSPLSM on the same moving speed.

(2) Compared with that of the TTWDSPLSM, the thrust density of the 120°-TWDSPLSM is increased by 21.62% on the similar magnetic load and electrical load.

(3) The efficiency of the 120°-TWDSPLSM is higher than that of TTWDSPLSM in various frequencies.

The primary drawback of the 120°-TWDSPLSM is the high detent force and thrust ripple. Therefore, the further optimization of the 120°-TWDSPLSM will be a future investigation and shall be reported soon.

ACKNOWLEDGMENT

This work is partially supported by Natural Science Foundation of China under grant No.51777060, in part by the Major Special Project for Collaborative Innovation in Zhengzhou No. 20XTZX12023.

REFERENCES

- [1] C. E. Kim, S. H. Lee, D. H. Lee, and H. J. Kim, "The analysis of permanent magnet double-sided linear synchronous motor with perpendicular arrangement," *IEEE Transactions on Magnetism*, vol. 49, no. 5, pp. 2267-2270, May 2013.
- [2] Y. S. Kwon and W. J. Kim, "Electromagnetic analysis and steady-state performance of double-sided flat linear motor using soft magnetic composite," *IEEE Transactions on Industrial Electronics*, vol. 64, no. 3, pp. 2178-2187, Mar. 2017.
- [3] Z. J. Zhang, M. Z. Luo, J. A. Duan, and B. Q. Kou, "Performance analysis of double-sided permanent magnet linear synchronous motor with quasi-sinusoidal ring windings," *IEEE Transactions on Energy Conversion*, vol. 35, no. 3, pp. 1465-1474, Sept. 2020.
- [4] B. Rezaeealam and F. Rezaeealam, "Optimization of permanent magnet synchronous motors using conformal mappings," *Applied Computational Electromagnetic Society (ACES) Journal*, vol. 32, no. 10, pp. 915-923, Oct. 2019.
- [5] G. D. Liu, Y. Z. Wang, X. P. Xu, W. Y. Ming, and X. Zhang, "The optimal design of real time control precision of planar motor," *Applied Computational Electromagnetic Society (ACES) Journal*, vol. 32, no. 10, pp. 948-954, Oct. 2019.
- [6] F. F. Bian, W. X. Zhao, J. H. Ji, L. Xu, H. Chen, and M. H. Gao, "Mechanism investigation of ring type winding in linear permanent magnet vernier machine for improving force density," *IEEE Transactions on Vehicular Technology*, vol. 69, no. 3, pp. 2588-2597, Mar. 2020.
- [7] A. Boduroglu, Y. Demir, B. Cumhur, and M. Aydin, "A novel track structure of double-sided linear PM synchronous motor for low cost and high force density applications," *IEEE Transactions on Magnetism*, DOI 10.1109/TMAG.3017448, 2021.
- [8] Y. Zhou, C. J. Shi, R. H. Qu, D. W. Li, and Y. T. Gao, "Overview of flux-modulation linear permanent magnet machines," *Proceeding of the CSEE*, vol. 41, no. 4, pp. 1469-1484, Feb. 2021.
- [9] C. J. Shi, R. H. Qu, Y. T. Gao, D. W. Li, L. B. Jing, and Y. Zhou, "Design and analysis of an interior permanent magnet linear vernier machine," *IEEE Transactions on Magnetism*, vol. 54, no. 11, pp. 1-5, June 2018.
- [10] L. Y. Li, M. N. Ma, B. Q. Kou, and Q. Q. Chen, "Analysis and design of moving-magnet-type linear synchronous motor for electromagnetic launch system," *IEEE Transactions on Plasma Science*, vol. 39, no. 1, pp. 121-126, Jan. 2011.
- [11] B. Q. Kou, H. X. Wu, L. Y. Li, L. L. Zhang, Z. Zhao, and H. C. Cao, "The thrust characteristics investigation of double-side plate permanent magnet linear synchronous motor for EML," *IEEE Transactions on Magnetism*, vol. 45, no. 1, pp. 501-505, Jan. 2009.
- [12] W. M. Tong, S. N. Wu, and R. Y. Tang, "Research on the airflow and thermal performance in a large forced air-cooled permanent magnet synchronous machine," *IEEE Access*, DOI 10.119/ACCESS.2951919, 2019.
- [13] Y. Q. Wang, X. Y. Huang, and Y. T. Fang, "Thermal analysis and cooling structure selection of electric machine applied in EV," *Micromotors*, vol. 53, no. 1, pp. 1-5, Jan. 2020.
- [14] W. B. Kong, J. Huang, R. H. Qu, M. Kang, and J. Q. Yang, "Nonsinusoidal power supply analysis for concentrated-full-pitch-winding multiphase induction motor," *IEEE Transactions on Industrial Electronics*, vol. 63, no. 1, pp. 574-582, Jan. 2016.

- [15] X. Z. Huang, T. P. Ji, L. Y. Li, B. Zhou, Z. R. Zhang, D. Gerada, and C. Gerada, "Detent force, thrust, and normal force of the short-primary double-sided permanent magnet linear synchronous motor with slot-shift structure," *IEEE Transactions on Energy Conversion*, vol. 34, no. 3, pp. 1411-1421, Sept. 2019.
- [16] S. W. Seo, G. H. Jang, J. M. Kim, and J. Y. Choi, "Characteristic analysis and experimental verification for a double-sided permanent magnet linear synchronous generator according to magnetization array," *IEEE Transactions on Applied Superconductivity*, DOI 10.1109/TASC. 2790941, 2018.
- [17] S. G. Lee, S. A. Kim, S. Saha, Y. W. Zhu, and Y. H. Cho, "Optimal structure design for minimizing detent force of PMLSM for a ropeless elevator," *IEEE Transactions on Magnetics*, DOI 10.1109/TMAG. 2277544, 2013.
- [18] H. Zhang, B. Q. Kou, Z. Q. Zhu, R. H. Qu, J. Luo, and Y. Shao, "Thrust ripple analysis on toroidal-winding linear permanent magnet vernier machine," *IEEE Transactions on Industrial Electronics*, vol. 65, no. 12, pp. 9853-9862, Dec. 2018.
- [19] C. X. Gao, M. Z. Gao, J. K. Si, Y. H. Hu, and C. Gan, "A novel direct-drive permanent magnet synchronous motor with toroidal windings," *Energies*, DOI 10.3390/en12030432, 2019.
- [20] M. C. Sun, R. Y. Tang, X. Y. Han, and W. M. Tong, "Analysis of open circuit back electromotive force in slotless toroidal type windings axial flux permanent magnet machine," *Electric Machine and Control Application*, vol. 44, no. 9, pp. 1-8. Sep. 2017.
- [21] S. L. Shi, E. L. Kang, and G. Y. Shi, "Optimization design of a permanent magnet linear motor using finite element and Taguchi method," *Micromotors*, vol. 53, no. 3, pp. 33-37, Mar. 2020.
- [22] S. L. Shi and E. L. Kang, "Electromagnetic design and performance analysis of permanent magnet synchronous linear motor," *Micromotors*, vol. 48, no. 3, pp. 25-28, July 2020.



Xiaobao Chai was born in China in 1997. He received B.S. degrees in Electrical Engineering and Automation, Electrical Engineering from the Department of Electrical Engineering and Automation, Shenyang University of Technology, China, in 2019. He is currently working toward the M.S. degree in Electrical Engineering from the Department of Electrical Engineering and Automation, Zhengzhou University, China. His current research interests include design, analysis and control of double-

sided permanent magnet linear synchronous motor.



Jikai Si received the B.S. degree in Electrical Engineering and Automation from the Jiaozuo Institute of Technology, Jiaozuo, China, in 1998; the M.S. degree in Electrical Engineering from Henan Polytechnic University, Jiaozuo, China, in 2005; and the Ph.D. degree in 2008 from the School of Information and Electrical Engineering, China University of Mining and Technology, Xuzhou, China, in 2008. He is currently a Distinguished Professor at Zhengzhou University. His main research interests include the theory, application, and control of special motor. He has authored and co-authored over 160 technical papers in these areas. Si is a Member of the Green Motor System Professional Committee, China.



Yihua Hu received the B.S. degree in Electrical Motor Drives, in 2003, and the Ph.D. degree in Power Electronics and Drives, in 2011, both from China University of Mining and Technology, Jiangsu, China. Between 2011 and 2013, he was a Postdoctoral Fellow with the College of Electrical Engineering, Zhejiang University, Zhejiang, China. He is currently a Distinguished Professor at University of York. His research interests include PV generation system, power electronics converters and control, and electrical motor drives.



Yingsheng Li currently works in Zhengzhou Runhua Intelligent Equipment Co., Ltd, and is the legal representative of Zhengzhou Runhua Intelligent Equipment Co., Ltd. His research interests include the application, control of motor, and power electronics converters and control, and electrical motor drives.



Dongshu Wang received the bachelor's degree in Mechanical Manufacture Technique and Equipment, the master's degree in Mechanical Manufacture and Automation, and the Ph.D. degree in Control Theory and Control Engineering from Northeastern University, Shenyang, China, in 1996, 2002, and 2006, respectively. He is currently an Associate Professor with the School of Electrical Engineering, Zhengzhou University, Zhengzhou, China. His research domains are autonomous mental development and artificial intelligence.